Magnesium transport in olivine mantle: new insights from miniaturized study of volume and grain boundary diffusion in Mg2SiO4 bi-crystals

Emmanuel Gardés, David Gibouin, Bertrand Radiguet, Adrian David, Wilfrid Prellier, Katharina Marquardt

Magnesium transport in olivine mantle: new insights from miniaturized study of volume and grain boundary diffusion in Mg_2SiO_4 bi-crystals

Emmanuel Gardés[a,*], David Gibouin[b], Bertrand Radiguet[b], Adrian David[c], Wilfrid Prellier[c], Katharina Marquardt[d]

[a] Normandie Université, ENSICAEN, CEA, CNRS, Centre de recherche sur les Ions, les Matériaux et la Photonique, 14000 Caen, France

[b] Normandie Université, UNIROUEN, INSA Rouen, CNRS, Groupe de Physique des Matériaux, 76000 Rouen, France

[c] Normandie Université, Laboratoire CRISMAT, CNRS UMR 6508, ENSICAEN, UNICAEN, 14000 Caen, France

[d] Department of Materials, Imperial College London, London, United Kingdom

[*] Corresponding author: gardes@ganil.fr

Abstract

We report experimental measurements of volume and grain boundary diffusion of ^{26}Mg in Mg_2SiO_4 bi-crystals at asthenosphere temperatures as a ground reference for olivine. By analysis of literature and combination with previous data, we provide Arrhenius laws $D = D_0 \exp(-E/RT)$ at ambient pressure for volume diffusion of Mg in Mg_2SiO_4 in the intrinsic regime along the three crystallographic axes as well as grain boundary diffusion. Parameters for average volume diffusion, calculated as geometrical mean of the three crystallographic axes, are

$D_0 = 10^{-2.12\pm0.91}$ m^2/s and $E = 443 \pm 42$ kJ/mol.

Parameters for average grain boundary diffusion in aggregate are

$D_0 = 10^{-1.16\pm0.49}$ m^2/s and $E = 359 \pm 14$ kJ/mol.

In the asthenosphere, the decrease of both volume and grain boundary diffusion coefficients as a function of pressure should remain negligible up to 1 GPa, and ~1 log unit at 10 GPa, while the increase in iron- and hydrogen-bearing olivine should range from ~1 to 2 log unit. The equilibration of Mg in olivine grains can be considered instantaneous with respect to geological timescales in the asthenosphere. However, the transport of Mg remains below km-scale even after 1 Gy at 1600°C of volume or grain boundary diffusion. Long-range transport of major elements in the upper mantle is not possible by solid-state diffusion. Equilibration of long-range heterogeneities and large mass transport is rather controlled by diffusion in intergranular fluid or melt phase, liquid percolation and mantle convection.

Keywords

Intragranular and intergranular mass transport, Upper mantle, Magnesium, Olivine, Volume diffusion, Grain boundary diffusion

Introduction

The diffusion of Mg in olivine is a prime process in upper mantle since Mg, with O and Si, is among the most abundant elements and olivine the most abundant mineral. Though mantle olivine contains iron, Mg_2SiO_4 constitutes the main component of the solid solution and diffusion in M-sites will mainly involve Mg movements. The study of Mg diffusion in Mg_2SiO_4 thus provides ground reference for diffusion in olivine. The diffusion of Mg and, generally speaking, the diffusion of M-site elements in both the volume and grain boundaries of olivine is involved, among others, in mass transfer and equilibration of chemical heterogeneities (Gardés and Heinrich, 2011; Gardés et al., 2012), water storage and cycling (Kohlstedt and Mackwell, 1998; Demouchy and Mackwell, 2006; Ingrin and Blanchard, 2006; Jollands et al., 2016), or electrical conductivity (Constable, 2006; Yoshino et al., 2009; Gardés et al., 2014).

While asthenosphere temperatures typically fall between 1300 and 1600°C, Mg diffusion in Mg_2SiO_4 was mostly investigated at lower temperatures. The highest temperature investigated during grain boundary diffusion experiments is 1300°C (Farver et al., 1994), and most of volume diffusion experiments were performed at temperatures below 1300°C (see data collection in Fig. 8 of Jollands et al., 2020). High temperature favours diffusion in the intrinsic regime where defects are produced by thermal agitation (Philibert, 1991). Contrastingly, the defect population for diffusion in the extrinsic regime is controlled by impurities. A typical example in mantle olivine is Fe substitution for Mg, which occurrence as Fe^{3+} correlates on oxygen fugacity fO_2 and implies the additional presence of defects for charge balancing (see e.g. Dohmen et al., 2007; Chakraborty, 2010 and references therein). Thus, depending on the impurity content and run conditions, diffusion in the extrinsic regime may lead to a broad range of diffusion coefficients which amplifies at low temperature, as observed for Mg diffusion in Mg_2SiO_4 (see data collection in Fig. 8 of Jollands et al., 2020 where part of scattering may also result from variable quality of measurement).

We report here measurements of volume and grain boundary diffusion of ^{26}Mg in Mg_2SiO_4 at 1300, 1400 and 1500°C at 1 atm in air. By combining bi-crystal synthesis, isotopic thin film deposition, focused ion beam machining and nanoscale secondary ion mass spectroscopy analysis, we developed a

protocol allowing for the simultaneous determination of volume diffusion in two directions and grain boundary diffusion on a single sample. From comparison with literature, we show volume diffusion occurred in the intrinsic regime. Combining our data to those from literature, we provide robust Arrhenius laws for volume diffusion along the three crystallographic axes, for their geometrical average, and for grain boundary diffusion. The effects of pressure, iron, and hydrogen are evaluated, and implications for Mg equilibration in mantle olivine grains as well as Mg transport in the upper mantle are finally discussed.

Experimental and analytical

Bi-crystal substrate

A high-purity single crystal of Mg_2SiO_4 was grown using the Czochralski technique (e.g. Müller, 2007) at the Leibniz-Institut für Kristallzüchtung (IKZ) in Berlin (see Electronic Supplementary Material 1 for trace element analysis). The crystal was oriented using X-ray diffraction, cut in ~300 µm thick wafers with ~1×1 cm^2 (016) faces, and polished down to sub-nanometric roughness with Ra < 0.34 nm by Crystal GmbH. A bi-crystal was produced by putting the (016) faces of two wafers into contact after 180° rotation of one wafer relative to the other (Fig. 1). The method, which includes a five-step cleaning and a three-step bonding with increasing temperatures up to 1650°C, is described in Hartmann et al. (2010). This bi-crystal was then cut into millimetric samples and their surfaces were polished down to 0.25 µm diamond and finally with colloidal silica. As seen schematically on a cross-section perpendicular to grain boundary (Fig. 1), the samples are such that (i) the surface planes on both sides of grain boundary are about normal to *b* axis (5.6° off; (061) planes), (ii) the grain boundary planes are about normal to *c* axis (5.6° off; (016) planes), and (iii) the grain boundary is a symmetric *a* axis tilt boundary (016)/[100] with 11.2° misorientation angle (see Adjaoud et al., 2012 for further geometrical and structural description).

Isotopic thin film

An isotopic source was prepared from commercial >99.5% ^{26}Mg-enriched MgO and >99.5% ^{29}Si-enriched SiO_2 powders. The powders were oven dried and mixed in proportions of Mg_2SiO_4 formula.

The mixture was crushed and homogenised in agate mortar, cold-pressed as 13 mm pellet, placed in a platinum crucible and sintered at 1400°C for 3 h in a horizontal furnace with an alumina tube. Pulsed laser deposition was used to deposit the isotopic source as a thin film on the surface of the bi-crystals. The isotope-doped pellet was ablated at room temperature and pressure of 10^{-4} mbar using a KrF excimer laser with a wavelength of 248 nm at a frequency of 3 Hz and a fluence of 1 J/cm^2.

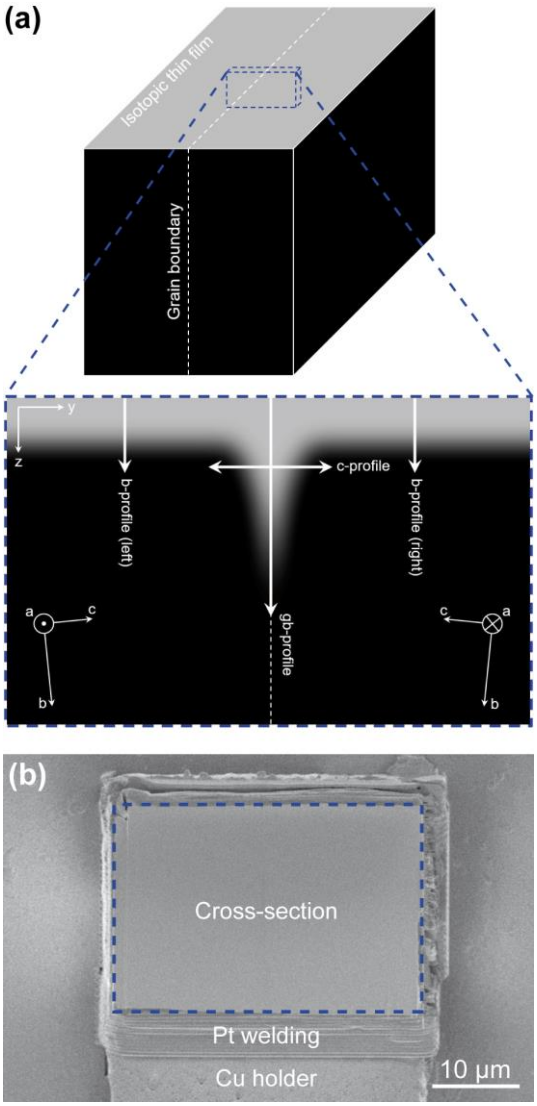

Fig. 1 Geometry of sample and analysis on cross-section. **a** Schematic of the isotope-enriched thin film lying at the top of the grain boundary of the bi-crystal. After diffusion annealing at high temperature, a cross-section is extracted perpendicular to grain boundary for mapping volume and grain boundary diffusion. The geometry is such that diffusion along *b* axis, *c* axis and grain boundary can be investigated from b-, c- and gb-profiles on a single cross-section. **b** Cross-section extracted from sample annealed at 1500°C for 2 h (SEM imaging)

Sample annealing

Prior to high temperature annealings, the samples were briefly annealed at 900°C for 10 min in a horizontal furnace with a silica tube filled with 800 mbar $^{18}O_2$. Diffusion annealings were then performed at 1300, 1400 and 1500°C at 1 atm in air in a horizontal furnace with an alumina tube. Samples were placed in a platinum crucible for each annealing. Despite multiple isotope enrichment, only results for Mg diffusion are reported here. Note that most of the enrichment in $^{18}O_2$, initially planned for investigating oxygen diffusion, vanished in air during heating in high temperature runs. ^{16}O composes ~93-98% of O in the thin film of high temperature samples.

Sample cross-section

Cross-sections, several tens of µm wide and several µm thick, were extracted from the surface perpendicular to grain boundary, welded with Pt on Cu holder and ion-beam polished using Secondary Electron Microscope-Focused Ion Beam (SEM-FIB) apparatus (Fig. 1). Electron-transparent thin cross-sections were extracted for scanning transmission electron microscopy (STEM) within the SEM-FIB. Energy Dispersive X-ray Spectroscopy (EDS) was also used to investigate sample chemistry.

Isotope mapping

Isotopic analyses were performed using a Secondary Ion Mass Spectrometer (SIMS) equipped with nano-sized primary ion beam (CAMECA NanoSIMS 50 ion probe instrument) (e.g. Allo et al., 2021). 8 keV Cs^+ beam was used to map the cross-sections with ~30 to 100 nm/pixel and probe currents ranging from ~1 to 2.5 pA (samples were first deposited with Au-Pd to make their surface conductive). ^{26}Mg and ^{24}Mg isotopes were detected as $^{26}Mg^{16}O$ and $^{24}Mg^{16}O$ species, respectively, with calibration such that sample regions away from diffusion zones matches natural abundance ($^{26}Mg/^{24}Mg = 0.1394$; Lide, 2005). ^{25}Mg was not detected but calculated from ^{24}Mg according to natural abundance ($^{25}Mg/^{24}Mg = 0.1266$; Lide, 2005). ^{16}O signal was also used for measuring probe size. The isotopic fraction of ^{26}Mg, referred to as X or $^{26}Mg/Mg$ in the following, is calculated from measurements as

$$X = \frac{N^{26}}{N^{24}+N^{25}+N^{26}}, \quad (1)$$

where N^i are the counts of *i*-Mg isotope.

Diffusion geometry

Following this experimental and analytical protocol, a single cross-section allows investigating volume diffusion in two perpendicular directions as well as grain boundary diffusion (Fig. 1). Away from grain boundary, the concentration profile from the thin film towards the substrate, i.e. b-profile in Fig. 1, corresponds to diffusion along about *b* axis (5.6° off). Across grain boundary, beneath volume diffusion from the surface, c-profile relates to diffusion along about *c* axis (5.6° off). Along grain boundary, gb-profile relates to diffusion along symmetric *a* axis tilt boundary (016)/[100] with 11.2° misorientation angle. As we will see later, c- and gb-profiles are interdependent since grain boundary diffusion is required for volume diffusion in adjacent grains to occur, while this process restrains grain boundary diffusion.

Results

Thin film

Initially amorphous, the thin film is composed of small crystallites after brief annealing at 900°C for 10 min (Fig. 2a). Its thickness is 500 ± 150 nm, where the deviations from mean value comes from surface roughness. The isotopic fraction of ^{26}Mg is 0.97 ± 0.03, thus the initial enrichment of thin film is almost complete (Fig. 3a). After annealing at high temperatures, no more crystallites are visible but the film crystallizes epitactically on the bi-crystal substrate and the grain boundary extends up to the surface of the sample (Fig. 2b). Residual pores and inclusions are visible at the original location of the thin film. These inclusions appear depleted in MgO and enriched in SiO_2 as indicated by EDS analysis across thin film (Fig. 2c). After annealing at high temperatures, ^{26}Mg diffused in the volume and the grain boundary of the samples and is depleted in the thin film (Fig. 3b-d).

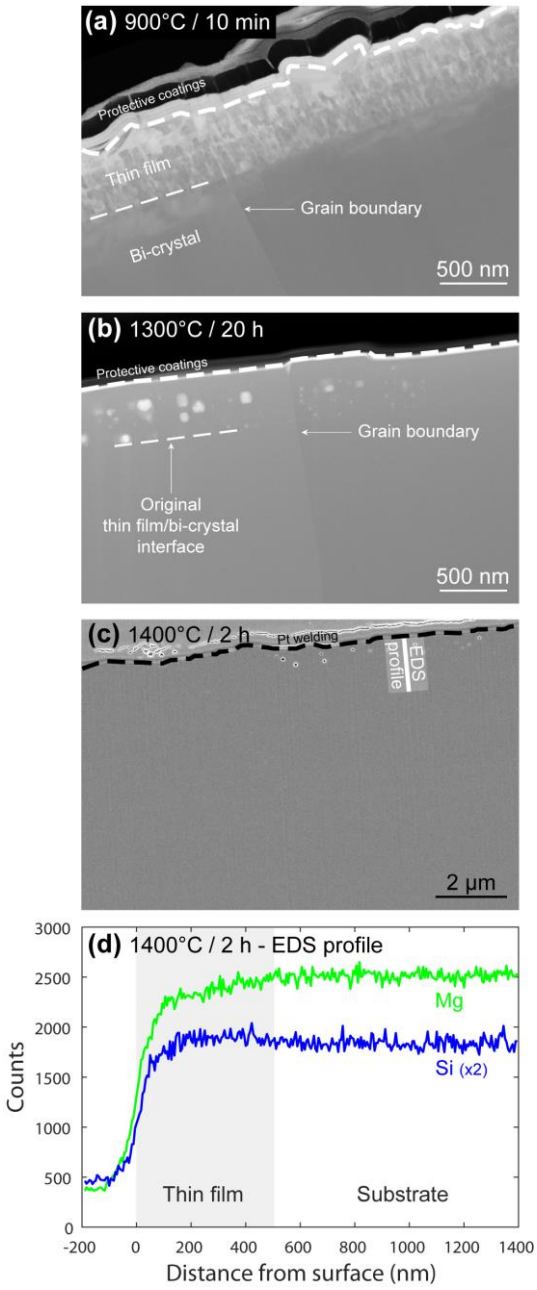

Fig. 2 Imaging and chemical analysis of sample cross-sections. Thin cross-sections of **a** sample after brief annealing at 900°C for 10 min and **b** sample after diffusion annealing at 1300°C for 20 h (30 kV STEM imaging; dashed lines delimit the surface of the samples). The thin film is made of crystallites at 900°C while epitaxy is complete and the bi-crystal extends up to sample surface at 1300°C. Residual pores and inclusions are visible at the original location of the thin film. **c** Thick cross-section of sample annealed at 1400°C for 2 h (SEM imaging; dashed line delimits the surface of the sample) and **d** associated EDS scan indicating the inclusions are depleted in MgO and enriched in SiO_2 (5 kV analysis; the thick line in **c** corresponds to position and length of the profile and shaded area corresponds to integration width).

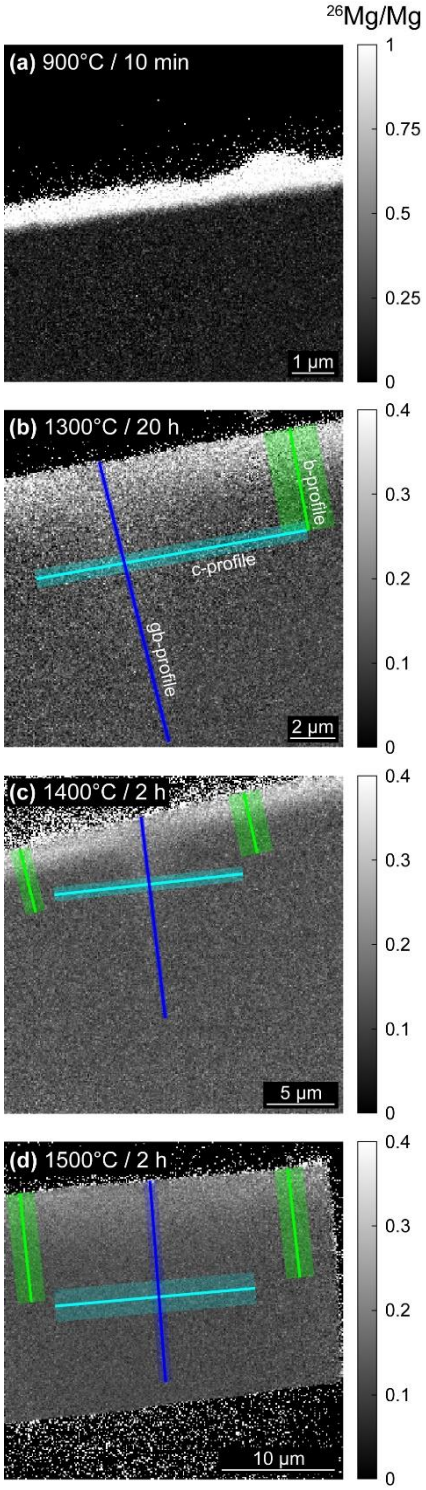

Fig. 3 Maps of ^{26}Mg isotopic fraction on sample cross-sections. **a** Brief annealing at 900°C for 10 min and diffusion annealing at **b** 1300°C for 20 h, **c** 1400°C for 2 h and **d** 1500°C for 2 h (nanoscale SIMS analysis). Volume and grain boundary diffusion is observed in all samples annealed at high temperatures **(c-d)**. Green, blue and cyan traverses correspond to b-, c- and gb-profiles used for diffusion modelling, respectively (thick line corresponds to position and length of the profile and shaded area corresponds to integration width).

Probe size

Before analysing diffusion profiles, we measured the size of the probe on each isotopic mapping as it may vary from one acquisition to the other, especially when the current is modified. We assume the ion beam to have a circular Gaussian shape

$$f(y,z) = \frac{1}{\pi\lambda^2}\exp\left(-\frac{y^2+z^2}{\lambda^2}\right), \quad (2)$$

where λ is a measurement of probe size, *y* and *z* are the directions parallel and perpendicular to sample surface on a cross-section, respectively (Fig. 1). In case of a linear measurement with probe size λ perpendicular to the interface of two homogeneous media, counts profile follows an error function (Electronic Supplementary Material 1)

$$N_\lambda(z) = \frac{N_\beta - N_\alpha}{2}\mathrm{erf}\left(\frac{z-z_0}{\lambda}\right) + \frac{N_\alpha + N_\beta}{2}. \quad (3)$$

where z_0 is the position of the interface, N_α are the counts in the medium located at $z < z_0$ (here platinum welding), N_β the counts in the medium at $z > z_0$ (here sample). The rise in ^{16}O signals across sample surface was refined with Eq. (3) to determine probe sizes λ, but also surface positions z_0 as both are required for modelling diffusion profiles (Fig. 4). λ ranges from ~100 to 220 nm for 1 to 2.5 pA acquisitions, respectively. It is worth noticing that Eq. (3) implies that more than 99.5% of the change during the traverse is reached at $z = z_0 + 2\,\lambda$ since erf(2) = 0.9953. Therefore signals from the sample at a distance longer than 2 λ from the surface can be considered unaffected by mixing with platinum welding (Fig. 4).

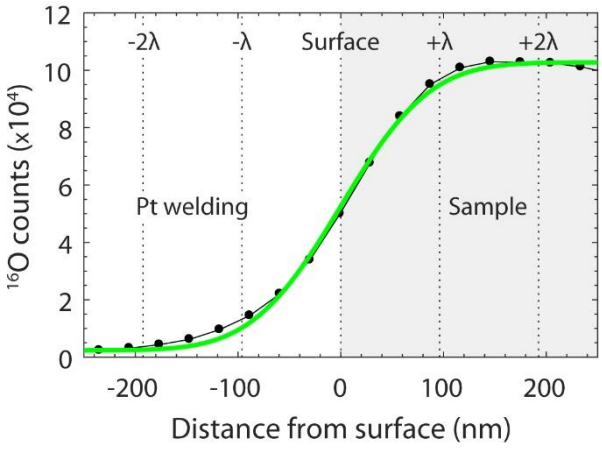

Fig. 4 Determination of probe size λ and position of sample surface. ^{16}O counts across the surface of the sample annealed at 1300°C for 20 h are adjusted with Eq. (3).

Volume diffusion along *b* axis

Volume diffusion along *b* axis is deduced from the profiles in ^{26}Mg isotopic fraction between thin film and substrate away from grain boundary, i.e. b-profiles (Figs. 1 and 3). This case corresponds to the diffusion between a film of finite thickness and a semi-infinite substrate with identical diffusion coefficient in both media since they have identical nature. In this geometry, the solution of diffusion equation yields for the isotopic fraction of ^{26}Mg (Crank, 1975; Gardés et al., 2006)

$$X_b(z) = \frac{X_0 - X_\infty}{2}\left(\mathrm{erf}\left(\frac{z - z_0 + h}{2\sqrt{D_b t}}\right) - \mathrm{erf}\left(\frac{z - z_0 - h}{2\sqrt{D_b t}}\right)\right) + X_\infty \text{ for } z > z_0 + 2\lambda, \quad (4)$$

where D_b is the diffusion coefficient along *b* axis, *h* the film thickness, *t* the annealing duration, X_0 the initial fraction of ^{26}Mg in the film, and X_∞ the initial fraction in the substrate, i.e. natural ^{26}Mg fraction. D_b was determined from best adjustments of Eq. 4 to b-profiles (Fig. 5) and uncertainties were estimated from adjustments where *h*, X_0^{26} and z_0 were drawn randomly within their confidence intervals (500 ± 150 nm, 0.97 ± 0.03 and z_0 ± 2 λ, respectively) (Table 1). Adjustments start at a distance of 2 λ from the surface to avoid the region where signals are mixed between sample and surrounding medium. Mean values for log D_b, with D_b in m^2/s, are -17.05 ± 0.06 at 1300°C, -16.02 ± 0.22 at 1400°C and -15.26 ± 0.11 at 1500°C (Table 1). No significant difference is found when

modelling b-profiles from each side of the grain boundary. Those values correspond to diffusion length $2\sqrt{D_b t}$ of 1.6 µm at 1300°C for 20 h, 1.7 µm at 1400°C for 2 h and 4.0 µm at 1500°C for 2 h. Note that the convolution with probe results in virtually no increase in the length of the diffusion profiles given present probe sizes, with differences between measured and actual log D_b remaining below 0.01 (Electronic Supplementary Material 1).

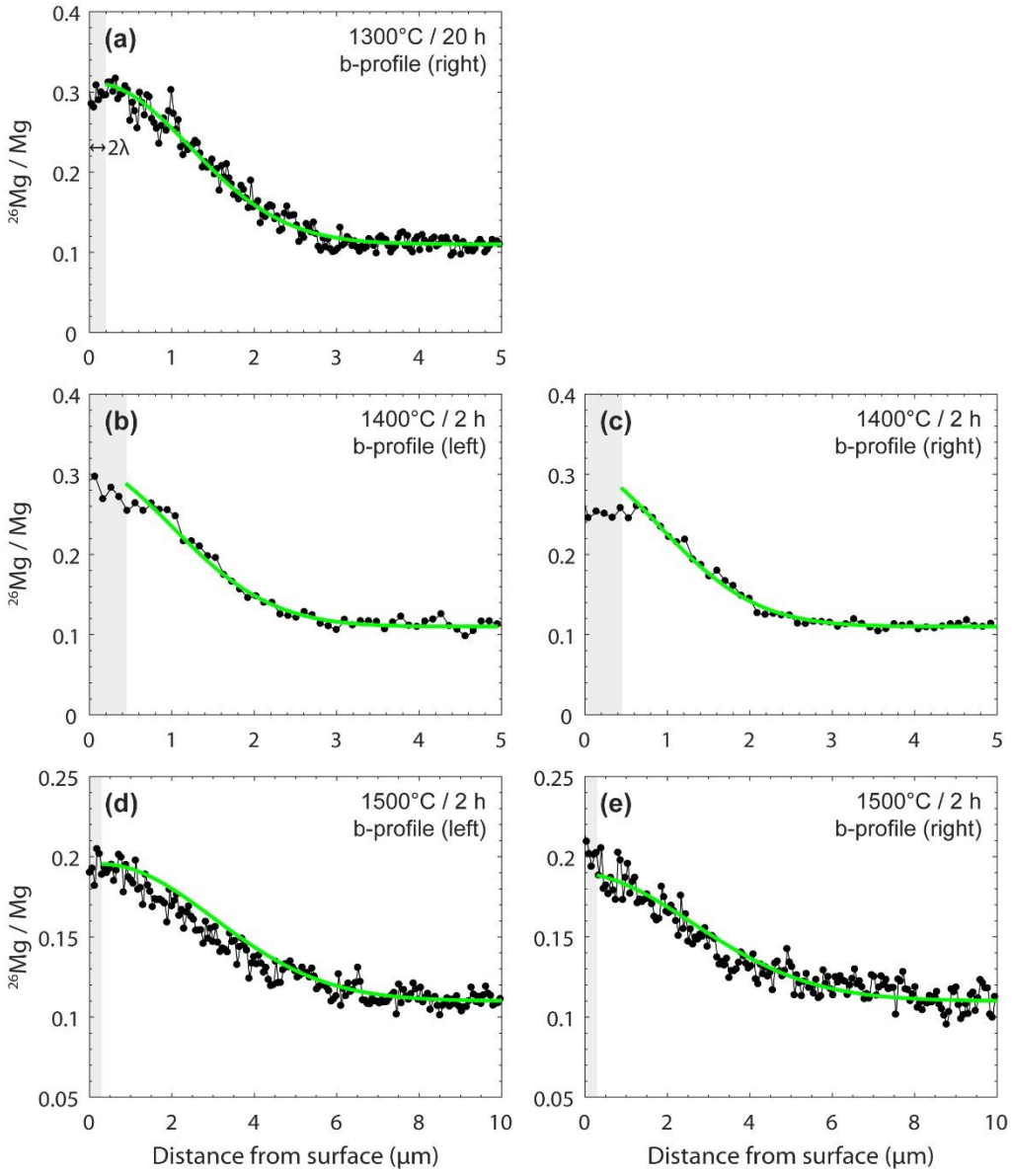

Fig. 5 Mg diffusion profiles of along *b* axis of Mg_2SiO_4. Adjustments with the solution of diffusion equation (Eq. 4) start for distance greater than 2 λ from surface, outside the grey regions, to avoid mixing of the signals with the surrounding medium.

Table 1 Diffusion coefficients of Mg along *b* axis, *c* axis and grain boundary of Mg_2SiO_4 given as log *D*, with *D* in m^2/s. Grain boundary diffusion coefficients are calculated considering a grain boundary width of 1 nm. The confidence intervals on the mean values for volume diffusion along *c* axis and grain boundary diffusion are such that they cover both constant source and instantaneous source solutions.

T (°C)	*t* (h)	Volume diffusion along *b* axis		
		Left profile	Right profile	Mean
1300	20	-	-17.05 ± 0.06	-17.05 ± 0.06
1400	2	-16.01 ± 0.19	-16.03 ± 0.25	-16.02 ± 0.22
1500	2	-15.29 ± 0.10	-15.24 ± 0.12	-15.26 ± 0.11
		Volume diffusion along *c* axis		
		Constant source	Instantaneous source	Mean
1300	20	-16.31	-16.74	-16.52 ± 0.21
1400	2	-15.23	-15.64	-15.44 ± 0.20
1500	2	-14.85	-15.03	-14.94 ± 0.09
		Grain boundary diffusion		
		Constant source	Instantaneous source	Mean
1300	20	-13.13	-12.94	-13.03 ± 0.09
1400	2	-12.20	-12.00	-12.10 ± 0.10
1500	2	-12.02	-11.65	-11.84 ± 0.18

Volume diffusion along *c* axis and grain boundary diffusion

Volume diffusion along *c* axis and grain boundary diffusion are deduced from the concomitant analysis of c-profiles across grain boundary and gb-profiles along grain boundary (Figs. 1, 3). Whipple (1954) and Suzuoka (1961) provided solutions to the problem of simultaneous diffusion along grain boundary and in the volume of adjacent grains for two different limit conditions. The solution of Whipple considers a diffusion source providing constant concentration at the surface of a bi-crystal, as would yield an infinitely thick source (Electronic Supplementary Material 1). On the other hand, the solution of Suzuoka considers an instantaneous, infinitely thin source (Electronic Supplementary Material 1). Our geometry lies in between these two cases since the dimension of the source is finite, with a film being smaller than diffusion lengths but not sufficiently small for being neglected. We thus bracket the analysis of diffusion profiles by using both Whipple and Suzuoka solutions, hereafter referred to as ‘constant source’ and ‘instantaneous source’ solutions, respectively. Away from the

surface region where diffusion across thin film and substrate along b-profiles superposes, i.e. farther than $h + 4\sqrt{D_b t}$ from surface, ^{26}Mg isotopic fraction in grain boundary region writes, according to the constant source solution (Electronic Supplementary Material 1)

$$X^{cs}(y,z) = \frac{X_0 - X_\infty}{4\sqrt{\pi}}\eta\int_1^\Delta \frac{1}{\sigma^{3/2}}\exp\left(-\frac{\eta^2}{4\sigma}\right)\mathrm{erfc}\left(\frac{1}{2}\sqrt{\frac{\Delta-1}{\Delta-\sigma}}\left(\xi + \frac{\sigma-1}{\beta}\right)\right)\mathrm{d}\sigma + X_\infty$$

for $z > z_0 + h + 4\sqrt{D_b t}$, (5)

and according to instantaneous source solution

$$X^{is}(y,z) = \frac{X_0 - X_\infty}{\sqrt{\pi D_c t}}h\int_1^\Delta \left(\frac{\eta^2}{4\sigma^{5/2}} - \frac{1}{2\sigma^{3/2}}\right)\exp\left(-\frac{\eta^2}{4\sigma}\right)\mathrm{erfc}\left(\frac{1}{2}\sqrt{\frac{\Delta-1}{\Delta-\sigma}}\left(\xi + \frac{\sigma-1}{\beta}\right)\right)\mathrm{d}\sigma + X_\infty$$

for $z > z_0 + h + 4\sqrt{D_b t}$, (6)

where

$\eta = \frac{z-z_0-h}{\sqrt{D_c t}}$, $\xi = \frac{|y-y_0|}{\sqrt{D_c t}}$, $\Delta = \frac{D_{gb}}{D_c}$ and $\beta = \frac{\Delta-1}{2\sqrt{D_c t}}\delta$. (7)

D_{gb} is the grain boundary diffusion coefficient and D_c is the diffusion coefficient in the volume of adjacent grains, i.e. the diffusion coefficient along *c* axis (Fig. 1). y_0 is the location of grain boundary along *y* axis. δ is the grain boundary width, considered hereafter to be 1 nm (e.g. Marquardt and Faul, 2018; Polednia et al., 2020). c-profiles at given $z = z_c > z_0 + h + 4\sqrt{D_b t}$ and gb-profiles along grain boundary at $y = y_0$ (Figs. 1, 3) were refined for determining D_c and D_{gb} concomitantly using the constant source solution (Eq. 5) on one hand, and the instantaneous source solution (Eq. 6) on the other hand (Fig. 6). Mean values from both solutions yields log D_c, with D_c in m^2/s, of -16.52 ± 0.21 at 1300°C, -15.44 ± 0.20 at 1400°C and -14.94 ± 0.09 at 1500°C where confidence intervals are such that they cover both solutions (Table 1). Similarly, mean values for log D_{gb} are -13.03 ± 0.09 at 1300°C, -12.10 ± 0.10 at 1400°C and -11.84 ± 0.18 at 1500°C (Table 1).

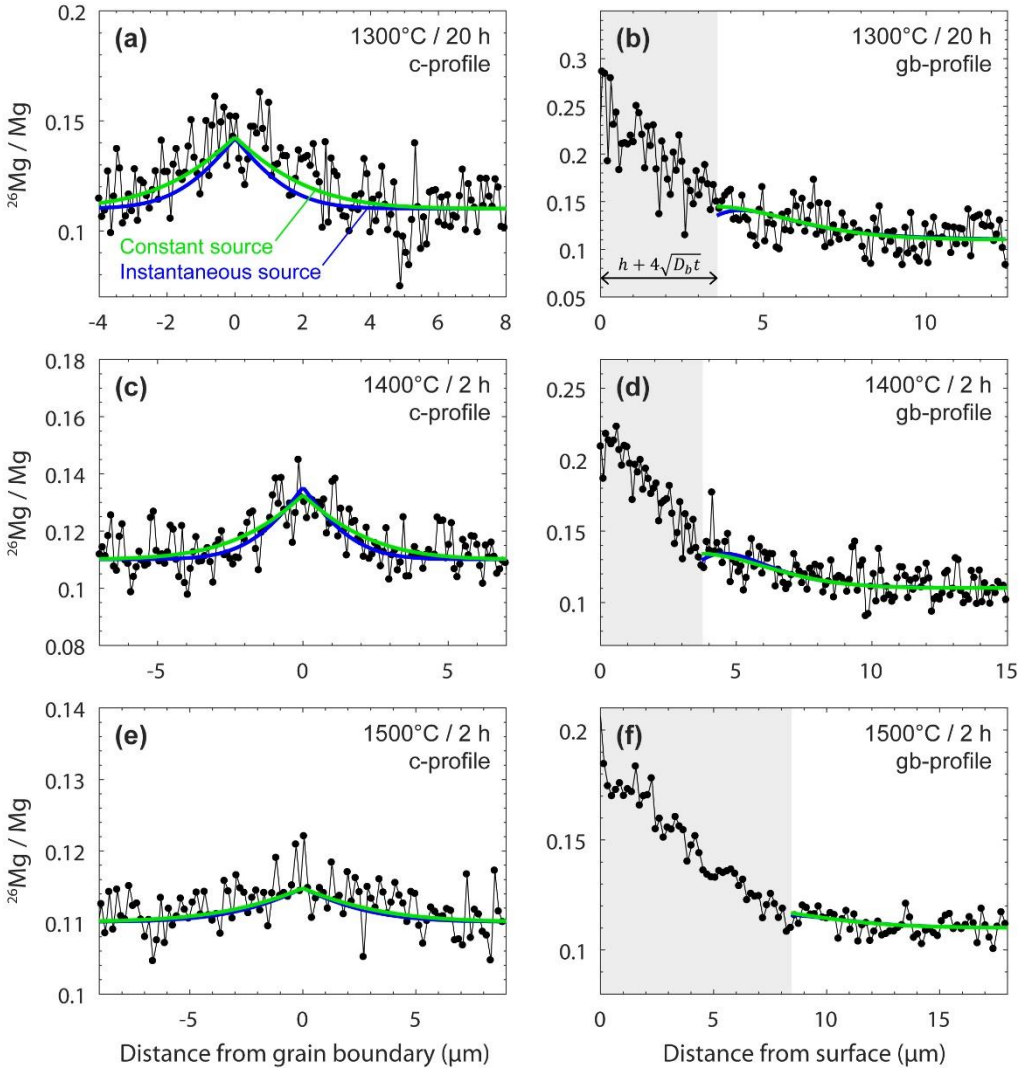

Fig. 6 Mg diffusion profiles **(a, c, e)** along *c* axis and **(b, d, f)** along grain boundary of Mg_2SiO_4. Adjustments with the solutions of diffusion equation in case of constant source (Eq. 5) and instantaneous source (Eq. 6) are reported as green and blues curves, respectively. In case of gb-profiles, adjustments start outside the grey regions where diffusion along *b* axis from the thin film to the substrate superposes, i.e. for distance longer than $h + 4\sqrt{D_b t}$ from surface. c-profiles across grain boundaries locate at 4.45, 4.75 and 10 µm from the surface for 1300, 1400 and 1500°C experiments, respectively, i.e. at distances from the surface longer than $h + 4\sqrt{D_b t}$.

Discussion

Volume diffusion

Comparison with experimental studies strongly indicates that our measurements represent diffusion in the intrinsic regime. Our data for volume diffusion along *b* and *c* axes are in very good agreement with the low silica activity dataset of the high temperature experiments (1250-1600°C) of Jollands et al. (2020) (Fig. 7). Their diffusion coefficients are independent on fO_2 over ~11 log unit up to 0.2 bar (as our experiments in air), and were interpreted to be representative of diffusion in the intrinsic regime (Muir et al., 2020). Our data for volume diffusion along *b* and *c* axes are also in line with the low oxygen fugacity dataset ($fO_2 = 10^{-12}$ bar) of the low temperature experiments (1000-1300°C) of Chakraborty et al. (1994) (Fig. 7). Note that Chakraborty et al. (1994) interpreted their data to represent diffusion in the extrinsic regime because the activation energy for diffusion of ~400 kJ/mol they measured was lower than the energy formation of intrinsic defects of ~800 kJ/mol estimated at that time. We will see below that this estimation was much too high. Even though part of the dataset of Chakraborty et al. (1994) does likely correspond to extrinsic diffusion, it appears from both our study and that of Jollands et al. (2020) that the measurements of Chakraborty et al. (1994) at the lowest oxygen fugacity $fO_2 = 10^{-12}$ bar do also represent intrinsic diffusion (Fig. 7). It is also worth noticing that the second part of the dataset of Jollands et al. (2020) at high silica activity ($aSiO_2$) yields ~1 log unit higher diffusion coefficients. In their computational study, Muir et al. (2020) interpret this as diffusion in an extrinsic regime involving Al impurity at high $aSiO_2$, already at play for ~1 wt. ppm Al_2O_3 at low temperature. However, though our thin film appears to be enriched in SiO_2, the 1.5 wt. ppm Al content was too low for this extrinsic mechanism to control diffusion in our high temperature experiments (Electronic Supplementary Material 1). Further insights into the combined effect of aluminium and silica activity on Mg diffusion in the extrinsic regime would require dedicated experiments with variable Al contents.

Our experimental data together with those of Jollands et al. (2020) at low $aSiO_2$ and those of Chakraborty et al. (1994) at low fO_2 thus follow a single trend from 1000 to 1600°C with no change in activation energy, as expected for diffusion in the intrinsic regime (Fig. 7). The refinements of these

data with Arrhenius laws $D = D_0 \exp(-E/RT)$ yield activation energies E of 395, 454 and 390 kJ/mol for diffusion along the *c*, *b* and *a* axes, respectively. The activation energy for diffusion along *c* axis is in excellent agreement with the 383 kJ/mol and 393 kJ/mol from the computational studies of Mg diffusion in pure Mg_2SiO_4 by Béjina et al. (2009) and Walker et al. (2009), respectively. This confirms these experimental data are representative of the intrinsic regime. Both simulations of Béjina et al. (2009) and Walker et al. (2009) yield that the migration of Mg occurs via vacancy mechanism and that the dominant intrinsic defects in Mg_2SiO_4 are Mg Frenkel pairs, with a ~320 kJ/mol formation energy. The agreement is less for *a* and *b* axes where Walker et al. (2009) calculated an activation energy of 513 kJ/mol for both axes, but there are much less experimental data at low temperature for precise determination of Arrhenius laws (Fig. 7). Thus, we propose to constrain the Arrhenius laws for *a* and *b* axes by combining experimental and computational results. Activation energy is taken as the average of that yielded by experimental data and that yielded by the simulations of Walker et al. (2009), with confidence interval covering both cases. Corresponding pre-exponential factor D_0 is obtained from refinement of experimental data. Arrhenius laws for Mg volume diffusion in Mg_2SiO_4 at 1 atm in the intrinsic regime have thus parameters

$D_0 = 10^{-3.19\pm0.88}$ m^2/s and $E = 395 \pm 26$ kJ/mol for diffusion along *c* axis, (8)

$D_0 = 10^{-0.86\pm0.92}$ m^2/s and $E = 483 \pm 30$ kJ/mol for diffusion along *b* axis, (9)

$D_0 = 10^{-2.30\pm0.92}$ m^2/s and $E = 451 \pm 62$ kJ/mol for diffusion along *a* axis, (10)

These laws do reproduce well the experimental data (Fig. 7). The mean absolute deviation over the whole database is 0.19 log unit, which compares with typical uncertainties on measurements of diffusion coefficients. It is of practical use to calculate the geometrical mean of diffusion coefficients along three axes, as it corresponds to volume diffusion in aggregates with randomly oriented grains (Fig. 8)

$D_0 = 10^{-2.12\pm0.91}$ m^2/s and $E = 443 \pm 42$ kJ/mol for average volume diffusion. (11)

Diffusion is fastest along *c* axis up to ~1700°C. Conversely, diffusion is slowest along *a* axis above ~900°C. The difference of each axis with geometrical mean remains below ~0.5 log unit above

1350°C. The anisotropy factor, i.e. the ratio of the diffusion coefficient along the fastest axis to that along the slowest axis, decreases as a function of temperature. It is ~1.5 log unit at 950°C, ~1 log unit at 1300°C and ~0.7 log unit at 1600°C. In the case of a deformed aggregate, the single crystal anisotropy factor of 1 log unit at 1300°C should produce aggregate anisotropy factors of about 0.3, 0.5 and 0.6 log unit at shear strains of 1, 2 and 4, respectively (Simpson and Tommasi, 2005).

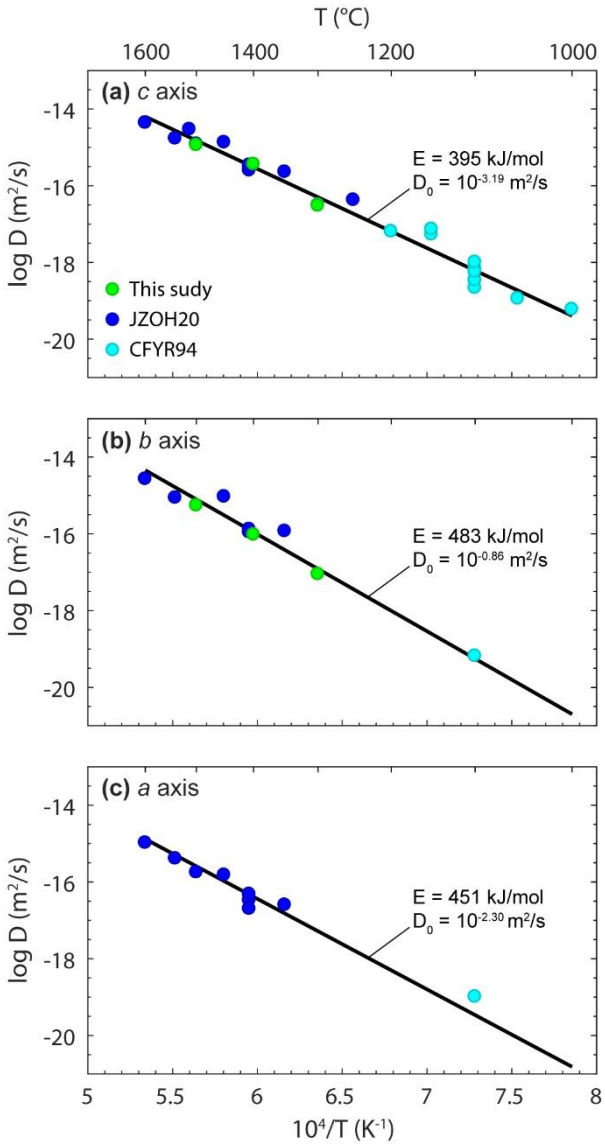

Fig. 7 Mg volume diffusion coefficient in Mg_2SiO_4 at 1 atm along **(a)** *c* axis, **(b)** *b* axis and **(c)** *a* axis. Experimental data from our study, from Jollands et al. (2020) at low $aSiO_2$ (JZOH20), and from Chakraborty et al. (1994) at low fO_2 (10^{-12} bar) (CFYR94). Black lines represent our model Arrhenius laws (Eqs. 8-10).

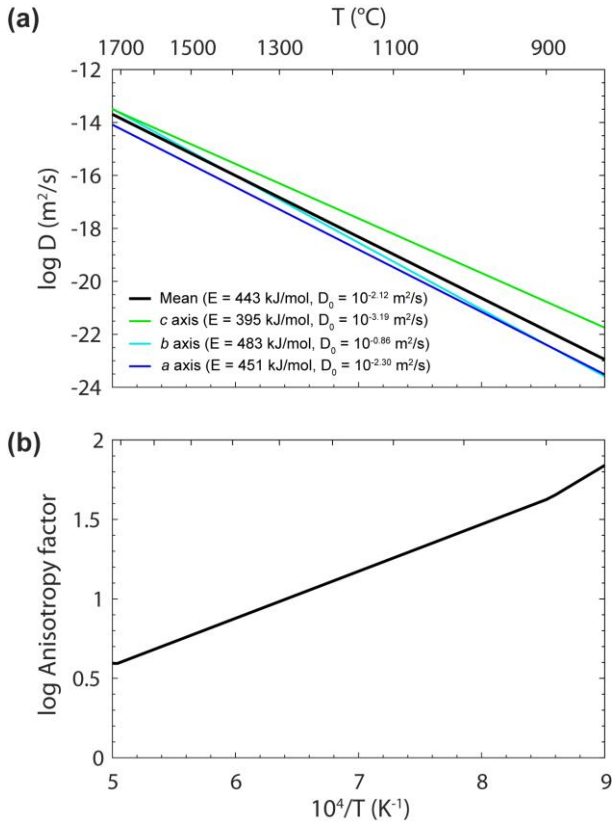

Fig. 8 Model Arrhenius laws for Mg volume diffusion coefficient in Mg_2SiO_4 at 1 atm. **a** Laws for the three crystallographic axes, together with geometrical mean as representative for volume diffusion in polycrystalline aggregates with randomly oriented grains (Eqs. 8-11). **b** Corresponding single crystal anisotropy factor.

Grain boundary diffusion

Farver et al. (1994) reported measurements of Mg grain boundary diffusion in polycrystalline aggregates of Mg_2SiO_4 at 1 bar with $fO_2 = 10^{-12}$ bar. Only their experiments using $CO+CO_2$ gas mixture are considered here as they interpreted their measurements with H_2+CO_2 mixture to be influenced by incorporation of H species. They calculated grain boundary coefficients from depth profiles following the relation of LeClaire (1963), using the geometrical mean of Chakraborty et al. (1994) data as volume diffusion coefficient. We thus recalculated their grain boundary diffusion coefficients using the geometrical mean provided here (Eq. 11). This yields ~0.3-0.5 log unit lower values than originally reported in Farver et al. (1994). Those values are in line with our grain boundary diffusion coefficients (Fig. 9).

In their computational study, Wagner et al. (2016) investigated Mg grain boundary diffusion in Mg_2SiO_4 for various grain boundary geometries. They found diffusion coefficients correlate on grain boundary excess volume, i.e. the difference between the volume of cells with and without grain boundary per area of grain boundary. Grain boundary diffusion coefficient increases by ~1.4 log unit when grain boundary excess volume increases from 0.34 to 1.3 $Å^3/Å^2$ at 1927°C. Wagner et al. (2016) simulated our specific symmetric *a* axis tilt boundary (016)/[100] with 11.2° misorientation angle at 1927°C. They found an intermediate grain boundary excess volume of 0.72 $Å^3/Å^2$ at 1927°C, yielding thus an intermediate diffusion coefficient. Two additional data representative of the (016)/[100] grain boundary can be obtained from the interpolations of their calculations at 1827°C and 1627°C at grain boundary excess volume of 0.72 $Å^3/Å^2$ (see Fig. 6 in Wagner et al. 2016). These values are also in line with our grain boundary diffusion coefficients (Fig. 9).

The agreement between our measurements, the calculation of Wagner et al. (2016) for identical (016)/[100] grain boundary and the measurements of Farver et al. (1994) in polycrystalline aggregates for temperatures spreading over ~900°C is remarkable. It demonstrates that the diffusion in the (016)/[100] grain boundary of our bi-crystals is a good representative of average grain boundary diffusion in polycrystalline aggregates with randomly oriented grains. The refinement of our data, those of Farver et al. (1994) and those of Wagner et al. (2016) yields the Arrhenius law for Mg grain boundary diffusion in Mg_2SiO_4 polycrystalline aggregates at 1 atm with parameters

$D_0 = 10^{-1.16\pm0.49}$ m^2/s and $E = 359 \pm 14$ kJ/mol for average grain boundary diffusion, (12)

when considering a grain boundary width of 1 nm (e.g. Marquardt and Faul, 2018; Polednia et al., 2020). It reproduces the data with a mean absolute deviation of 0.11 log unit. Following Wagner et al. (2016), diffusion coefficient in a given grain boundary may deviate by about ±0.5 log unit from this average law as a function of its excess volume (Fig. 9).

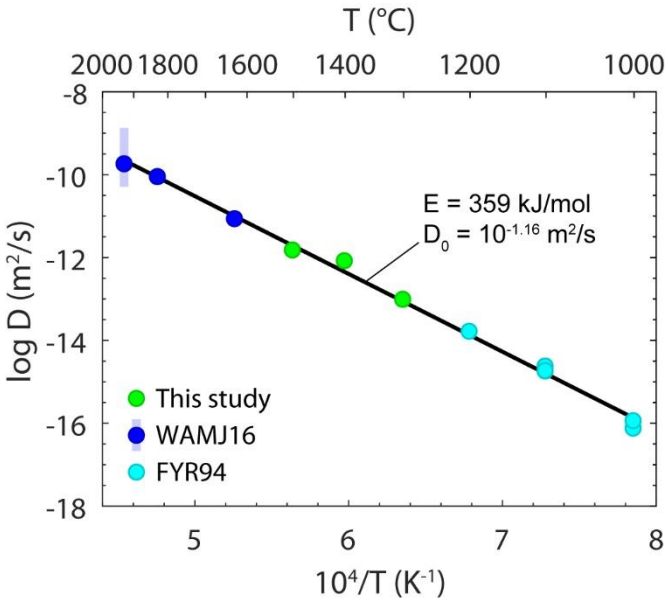

Fig. 9 Mg grain boundary diffusion coefficient in Mg_2SiO_4 at 1 atm. Experimental data from our study, from Farver et al. (1994) with $CO+CO_2$ gas mixture (FYR94), and calculations from Wagner et al. (2016) for (016)/[100] grain boundary identical to our samples (WAMJ16; the blue rectangle indicate the range yielded by the other grain boundary geometries investigated) . Black line represents our model Arrhenius law (Eq. 12). A grain boundary width of 1 nm was considered.

Effect of pressure, iron and hydrogen

The effect of pressure on diffusion is usually small compared to temperature. All studies reported a negative effect of pressure, i.e. positive activation volume, on Mg diffusion in both volume and grain boundaries of Mg_2SiO_4. For volume diffusion, activation volumes are 1-3.5 cm^3/mol from the experiments of Chakraborty et al. (1994), 4.3 cm^3/mol from the experiments of Fei et al. (2018a), and 5 cm^3/mol from the calculations of Béjina et al. (2009). Considering an average value of 3.9 cm^3/mol, and for temperatures of 1300-1600°C in the range of asthenosphere, the decrease of volume diffusion coefficients would remain negligible up to 1 GPa, since below ~0.12 log unit. The decrease would reach ~0.35 log unit at 3 GPa, and ~1.2 log unit at 10 GPa. For grain boundary diffusion coefficients, activation volumes are 1 cm^3/mol from the experiments of Farver et al. (1994) and 3.9 cm^3/mol from the experiments of Fei et al. (2018b). With an average value of 2.5 cm^3/mol and in the range of 1300-

1600°C, the decrease of grain boundary diffusion coefficient would remain negligible up to 1.5 GPa, below ~0.11 log unit. The decrease would reach ~0.23 log unit at 3 GPa, and ~0.8 log unit at 10 GPa.

The presence of Fe^{3+} in iron-bearing olivine is accompanied by defects additional to intrinsic defects. Contrary to pressure, the effect of Fe in olivine is thus to enhance volume diffusion. For instance, the diffusion coefficient is increased by about 1 to 2.5 log unit at 1300°C for fO_2 covering the stability field of iron-bearing olivine (see Dohmen et al. 2007 or Chakraborty 2010 for further details). There are no data for Mg grain boundary diffusion in Fe-bearing olivine. One might suppose a priori that the effect of Fe is to enhance grain boundary diffusion similarly to volume diffusion. However, since grain boundary diffusion depends on grain boundary excess volume (Wagner et al., 2016), it is possible that the effect of Fe remains weak or even negligible since both structures of Fe-bearing and Fe-free olivines are identical, with cell volumes differing by less than 1% between $(Mg_{0.9}Fe_{0.1})_2S_iO_4$ and Mg_2SiO_4 (Morrison et al., 2018).

Hydrogen incorporation in olivine occurs in the form of various defects (see Demouchy, 2021 and references therein) and results in further enhancement of Mg diffusion. At water-saturated conditions, Hier-Majumder et al. (2005) reported ~1 log unit increase in Fe-Mg volume interdiffusion in iron-bearing olivine. For instance, at 1200°C, 0.3 GPa and oxygen fugacity buffered at Ni-NiO, Fe-Mg interdiffusion coefficient along *c* axis is $10^{-16.3}$ m^2/s in anhydrous conditions while $10^{-15.5}$ m^2/s for water saturation. Those are respectively ~1 and ~2 log unit higher than the value of $10^{-17.2}$ m^2/s for Mg diffusion in anhydrous and iron-free olivine along *c* axis according to our law. In experiments of Mg grain boundary diffusion in Mg_2SiO_4, Farver et al. (1994) reported a ~0.7 log unit increase in annealings with H_2+CO_2 gas mixture relative to CO+CO_2 gas mixture, and Fei et al. (2018b) reported 1 to 2 log unit increases over broad ranges of hydrogen incorporation. Thus, apart from highly oxidising and highly hydrous environments, combined effect of Fe and H should mostly result in a 1 to 2 log unit increase for both volume and grain boundary diffusion of Mg in mantle olivine. As we will see below, the main effect of H_2O and other volatiles on mass transport is likely to favour the production of liquid phases in which diffusion is strongly enhanced relative to solids.

Implications for the upper mantle

When a concentration change is imposed to the surface of a grain, the characteristic time for its equilibration by diffusion is (Carslaw and Jaeger, 1959; Gardés and Montel, 2009; Electronic Supplementary Material 1)

$$\tau_{grain} = \alpha_{grain}\, d^2/D, \quad (13)$$

where α_{grain} = 6.33 10^{-2} for 95% equilibration of a spherical grain of diameter d. In the asthenosphere, equilibration of Mg in olivine grain with 1 mm diameter would require 140 years at 1300°C and 7 months at 1600°C according to our volume diffusion law (Fig. 10a). Equilibration time is much shorter when only the rim of the grain is considered (Electronic Supplementary Material 1)

$$\tau_{rim} = \alpha_{rim}\, d^2/D, \quad (14)$$

where α_{rim} = 2.23 10^{-3} for 95% equilibration of a rim with width taken as 1% of grain diameter d. Mg equilibration then reduces to 5 years at 1300°C and 8 days at 1600°C for the first 10 µm rim of a 1 mm grain (Fig. 10b). On the other hand, the characteristic time for equilibrating Mg in a grain boundary from adjacent grains is (Electronic Supplementary Material 1)

$$\tau_{gb} = \alpha_{gb}\, \delta^2/D_{gb}, \quad (15)$$

where α_{gb} = 2.82 10^{-1} for 95% equilibration of a grain boundary with width δ. This time is virtually zero, being below 10 µs for temperatures above 1300°C according to our grain boundary diffusion law (Fig. 10c). Following previous discussion, at asthenosphere temperatures, these equilibration times would be virtually unchanged up to ~1 GPa, decreased by a factor of ~2 at 3 GPa, and a factor of ~10 at 10 GPa in the range of asthenosphere temperatures of 1300-1600°C. In iron- and hydrogen-bearing olivine, 1 to 2 log unit higher volume diffusion coefficients imply 1 to 2 log unit decreases in grain equilibration times, while grain boundary diffusion is probably unchanged. Thus, the equilibration of Mg in mantle olivine grains from the asthenosphere is instantaneous with respect to geological timescales. Equilibration could however be questioned in part of the lithosphere where much lower

temperatures may require durations longer than 1 My for complete grain equilibration. Equilibration could then be limited to the rim of the grains (Fig. 10).

The characteristic lengths of Mg diffusion $2\sqrt{Dt}$ in both volume and grain boundary of olivine according to our diffusion laws are reported in Fig. 11 for various temperatures and durations. For instance, after 1 ky at 1300 to 1600°C, diffusion lengths are about 1 mm to 2 cm for volume diffusion and about 10 cm to 1 m for grain boundary diffusion. Thus volume diffusion acts at the scale of individual or adjacent grains and grain boundary acts at the scale of a few hundred grains at short timescale in the asthenosphere. It is worth mentioning that these lengths should be virtually unchanged up to ~1 GPa, decreased by a factor of ~1.4 at 3 GPa and a factor of ~3 at 10 GPa. In iron- and hydrogen-bearing olivine, 1 to 2 log unit higher diffusion coefficients should increase volume and grain boundary diffusion lengths by factor ~3 to ~10. Diffusion lengths remain below 100 m for volume diffusion and below 1 km for grain boundary diffusion after up to 1 Gy diffusion at 1600°C (Fig. 11). It is thus obvious that long-range Mg equilibration in the mantle is not possible by solid-state diffusion, either in volume or grain boundaries. Mg is part of the most abundant elements in the mantle together with O and Si. These latter elements diffuse even slower than Mg (see review by Chakraborty 2010). Long scale, large mass transport in the mantle is therefore not possible by solid-state diffusion.

The presence of volatiles such as H_2O and CO_2 in the mantle favours the production of fluids and melts in the mantle. For instance, as volatile contents spread around averages of 240 wt. ppm H_2O and 140 wt. ppm CO_2, melt fractions are estimated to range around 10^{-3} in the mantle, with fractions of carbonated melt down to ~10^{-4} in the lithosphere and fractions of basaltic melt up to ~10^{-1} in the asthenosphere beneath mid-ocean ridges (Le Voyer et al., 2017; Massuyeau et al., 2021). An intergranular liquid phase constitutes a fast transport pathway which may enhance bulk diffusivities in mantle rocks by several orders of magnitude, even for minute amounts of aqueous fluids (Gardés et al., 2012; Milke et al., 2013) or melts (Gardés et al., 2020). In an aggregate with intergranular liquid, bulk diffusion results from the superposition of solid-state diffusion in both grain volume and grain boundaries (Electronic Supplementary Material 1)

$$D_{bulk}^{solid} = (1-\varphi)\left(D + 2\frac{\delta}{d}D_{gb}\right), \quad (16)$$

and diffusion in the intergranular liquid (Electronic Supplementary Material 1)

$$D_{bulk}^{liquid} = \frac{1}{3}\varphi D_{liquid}, \quad (17)$$

where φ is the volume fraction of liquid and D_{liquid} is the diffusion coefficient in the liquid. We calculated D_{bulk}^{solid} according to our Arrhenius laws for volume and grain boundary diffusion of Mg in Mg_2SiO_4 (Eqs. 11 and 12), and considering a grain size of 1 mm and a grain boundary width of 1 nm. D_{bulk}^{liquid} was calculated for H_2O-rich fluid, CO_2-rich melt and SiO_2-rich melt according to Mg tracer diffusion in H_2O (Oelkers and Helgeson, 1988), Mg diffusion in molten $MgCO_3$ carbonate (Desmaele et al., 2019), and Mg diffusion in basalt (Chen and Zhang, 2008), respectively. Fig. 12 reports the liquid fractions where D_{bulk}^{liquid} equals D_{bulk}^{solid} for the various intergranular liquids, delimiting thus the domains where transport is controlled by solid-state or liquid-state diffusion. It is found that the control by liquid-state diffusion over solid-state diffusion occurs at very small fractions of liquid. The volume fraction above which H_2O-rich fluids control bulk diffusion in the lithosphere is virtually zero, being lower than 10^{-12} for temperatures below 1000°C. In case of CO_2-rich melts, the transition occurs at extremely small liquid fractions below ~10^{-8} for temperatures below 1300°C in the lithosphere, and in the range of 10^{-8}-10^{-5} for 1300-1600°C in the asthenosphere. The highest liquid fractions at which transition occurs are for SiO_2-rich melts in the asthenosphere, though remaining in the range of 10^{-6}-10^{-4}. It is worth recalling that the decrease of solid-state diffusion by ~1 log unit with increasing pressure to 10 GPa and the increase by ~1-2 log unit in iron- and hydrogen-bearing olivine would shift the transitions to ~1 log unit lower and ~1-2 log unit higher liquid fractions, respectively. Thus, diffusion in intergranular liquids should control bulk rock diffusion as soon as liquids are produced in most of mantle settings. Moreover, mantle convection requires 1 My to achieve 1-10 km displacements with 0.1-1 cm/y velocities, when reaching km-scale requires more than 1 Gy of solid-state diffusion. Partial melts can reach up to ~10 cm/y velocities when they are mobilized (Gaillard et al., 2019). Advective processes such as mantle convection and liquid percolation are thus also much more efficient for large mass transport and equilibration of long scale heterogeneities. However, solid-

state diffusion does allow for the equilibration of grain interiors and for the exchanges with adjacent grains and intergranular medium.

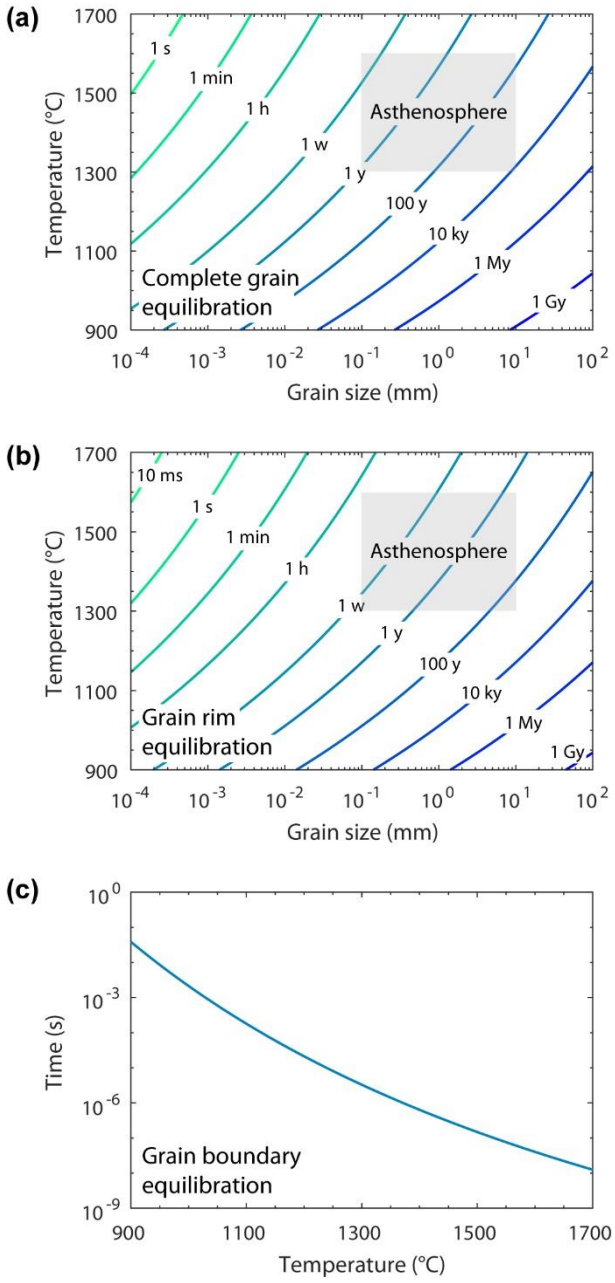

Fig. 10 Characteristic times of Mg equilibration by diffusion in **a** complete grain, **b** grain rim and **c** grain boundary of Mg_2SiO_4 at 1 atm. Times should be similar up to ~1 GPa, and increased by factor up to ~10 up to 10 GPa at asthenosphere temperatures of 1300-1600°C. In iron- and hydrogen-bearing olivine, times should be decreased by 1 to 2 log unit for both volume and grain boundary diffusion (see Text). Mg equilibration in olivine grains and adjacent grain boundaries is thus instantaneous in front of geological timescales at asthenosphere temperatures and grain sizes. Rim width defined as 1% of grain diameter, grain boundary width taken as 1 nm.

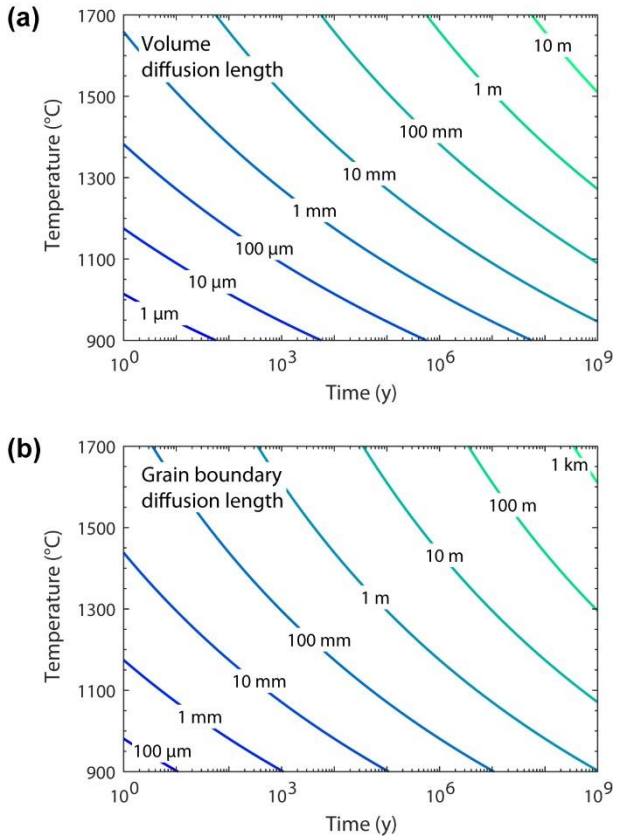

Fig. 11 Characteristic lengths of Mg diffusion in **a** volume and **b** grain boundary of Mg_2SiO_4 at 1 atm. Lengths should be similar up to ~1 GPa, and decreased by factor up to ~3 up to 10 GPa at asthenosphere temperatures of 1300-1600°C. In iron- and hydrogen-bearing olivine, lengths should be increased by factor ~3-10 for both volume and grain boundary diffusion (see Text). Long-range transport of Mg in the mantle via solid-state, volume or grain boundary diffusion is precluded since km-scale is not reached even after 1 Gy at 1600°C. At short timescale of ~1 ky in the asthenosphere, volume diffusion rather acts at the scale of individual or adjacent grains and grain boundary diffusion may allow exchanges between a few hundred grains.

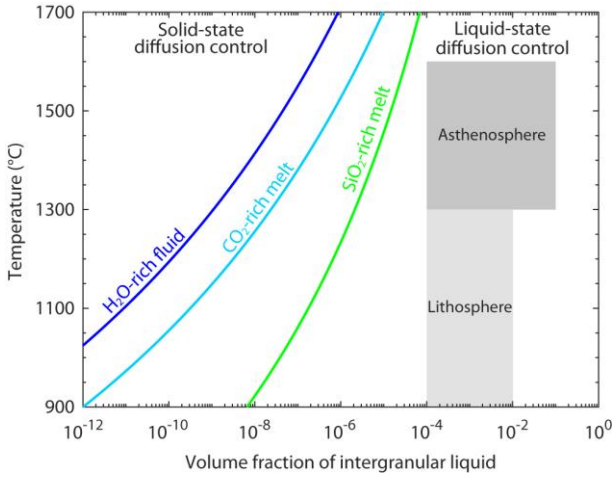

Fig. 12 Transition from solid-state to liquid-state control of Mg diffusion in olivine aggregate bearing H_2O-rich fluid, CO_2-rich melt or SiO_2 rich-melt. Liquid-state diffusion overcomes solid-state diffusion from very small fractions of liquid. Decrease of Mg solid-state diffusion by ~1 log unit at 10 GPa and increase by ~1-2 log unit in iron- and hydrogen-bearing olivine should shift the transitions to ~1 log unit lower and ~1-2 log unit higher liquid fractions, respectively. Comparison with typical melt fractions and temperatures for lithosphere and asthenosphere indicates that mass transport in intergranular liquids should control bulk diffusion as soon as liquids are produced in most of mantle settings.

Conclusion

We measured Mg diffusion in both volume and grain boundary of Mg_2SiO_4 bi-crystals from 1300 to 1500°C in air at 1 atm. Volume diffusion occurred in the intrinsic regime, where defects result from thermal agitation. Our results are in line with previous experimental and computational studies in the intrinsic regime, with a single Arrhenius law and thus single mechanism from 1000 to 1600°C. This agreement confirms the findings of computational studies that the migration of Mg occurs via vacancy mechanism and that the dominant intrinsic defects in Mg_2SiO_4 are Mg Frenkel pairs. Grain boundary diffusion coefficients in our bi-crystals are in line with previous computational study with identical grain boundary and experimental study in Mg_2SiO_4 aggregate. Our specific symmetric *a* axis tilt boundary (016)/[100] appears to be a good representative of average grain boundary diffusion in aggregates with randomly oriented grains.

The combination of our experimental data with previous experimental and computational data yields Arrhenius laws $D = D_0 \exp(-E/RT)$ with parameters

$D_0 = 10^{-3.19\pm0.88}$ m^2/s and E = 395 ± 26 kJ/mol for volume diffusion along *c* axis,

$D_0 = 10^{-0.86\pm0.92}$ m^2/s and E = 483 ± 30 kJ/mol for volume diffusion along *b* axis,

$D_0 = 10^{-2.30\pm0.92}$ m^2/s and E = 451 ± 62 kJ/mol for volume diffusion along *a* axis,

$D_0 = 10^{-2.12\pm0.91}$ m^2/s and E = 443 ± 42 kJ/mol for average volume diffusion,

$D_0 = 10^{-1.16\pm0.49}$ m^2/s and E = 359 ± 14 kJ/mol for average grain boundary diffusion.

For temperatures of 1300-1600°C in the range of asthenosphere, the decrease of both volume and grain boundary diffusion coefficients as a function of pressure would remain negligible up to 1 GPa, about 0.3 log unit at 3 GPa, and about 1 log unit at 10 GPa. In iron- and hydrogen-bearing olivine, the increase in the diffusion coefficients would range from about 1 to 2 log unit.

Mg equilibrates instantaneously compared to geological timescales in olivine grains from the asthenosphere. However, transport of Mg in the upper mantle via solid-state, volume or grain boundary diffusion remains below the km-scale even after 1 Gy at 1600°C. This also applies to O and Si as they diffuse even slower than Mg. Liquid-state diffusion should overcome solid-state diffusion as soon as liquids are produced in most of mantle settings. Diffusion in intergranular fluid or melt phase, liquid percolation and mantle convection are much more efficient in equilibrating long scale heterogeneities and transporting large mass.

References

Adjaoud O, Marquardt K, Jahn S (2012) Atomic structures and energies of grain boundaries in Mg_2SiO_4 forsterite from atomistic modelling. Phys Chem Minerals 39:749–760

Allo J, Jouen S, Roussel M, Gibouin D, Sauvage X (2021) Influence of sulfur and water vapor on high-temperature oxidation resistance of an alumina-forming austenitic alloy. Oxid Met 95:359–376

Béjina F, Blanchard M, Wright K, Price GD (2009) A computer simulation study of the effect of pressure on Mg diffusion in forsterite. Phys Earth Planet Inter 172:13–19

Carslaw HS, Jaeger JC (1959) Conduction of heat in solids, second ed. Oxford Science Publications, Oxford

Chakraborty S, Farver JR, Yund RA, Rubie DC (1994) Mg tracer diffusion in synthetic forsterite and as a function of P, T and fO_2. Phys Chem Minerals 21:489–500

Chakraborty S (2010) Diffusion coefficients in olivine, wadsleyite and ringwoodite. Rev Mineral Geochem 72:603–639

Chen Y, Zhang Y (2008) Olivine dissolution in basaltic melt. Geochim Cosmochim Acta 72:4756–4777

Constable S (2006) SEO3: A new model of olivine electrical conductivity. Geophys J Int 166:435–437

Crank J (1975) The Mathematics of Diffusion, second ed. Oxford University Press

Demouchy S (2021) Defects in olivine. Eur J Mineral 33:249–282

Demouchy S, Mackwell SJ (2006) Mechanisms of hydrogen incorporation and diffusion in iron-bearing olivine. Phys Chem Minerals 33:347–355

Desmaele E, Sator N, Vuilleumier R, Guillot B (2019) The $MgCO_3$–$CaCO_3$–Li_2CO_3–Na_2CO_3–K_2CO_3 melts: Thermodynamics and transport properties by atomistic simulations. J Chem Phys 150:214503

Dohmen R, Becker HW, Chakraborty S (2007) Fe–Mg diffusion in olivine I: experimental determination between 700 and 1,200°C as a function of composition, crystal orientation and oxygen fugacity. Phys Chem Minerals 34:389–407

Farver JR, Yund RA, Rubie DC (1994) Magnesium grain boundary diffusion in forsterite aggregates at 1000°-1300°C and 0.1 MPa to 10 GPa. J Geophys Res 99:19809–19819

Fei H, Koizumi S, Sakamoto N, Hashiguchi M, Yurimoto H, Marquardt K, Miyajima N, Katsura T (2018a) Mg lattice diffusion in iron-free olivine and implications to conductivity anomaly in the oceanic asthenosphere. Earth Planet Sci Lett 484:204–212

Fei H, Koizumi S, Sakamoto N, Hashiguchi M, Yurimoto H, Marquardt K, Miyajima N, Katsura T (2018b) Pressure, temperature, water content, and oxygen fugacity dependence of the Mg grain-boundary diffusion coefficient in forsterite. Am Mineral 103:1354–1361

Gaillard F, Sator N, Gardés E, Guillot B, Massuyeau M, Sifré D, Hammouda T, Richard G (2019) The link between the physical and chemical properties of carbon-bearing melts and their application for geophysical imaging of Earth's mantle. In: Orcutt B, Daniel I, Dasgupta R (eds) Deep Carbon: Past to Present, Cambridge University Press, pp 163–187

Gardés E, Jaoul O, Montel JM, Seydoux-Guillaume AM, Wirth R (2006) Pb diffusion in monazite: An experimental study of $Pb^{2+} + Th^{4+} \leftrightarrow 2Nd^{3+}$ interdiffusion. Geochim Cosmochim Acta 70:2325–2336

Gardés E, Montel JM (2009) Opening and resetting temperatures in heating geochronological systems. Contrib Mineral Petrol 158:185–195

Gardés E, Heinrich W (2011) Growth of multilayered polycrystalline reaction rims in the $MgO–SiO_2$ system, part II: modelling. Contrib Mineral Petrol 162:37–49

Gardés E, Wunder B, Marquardt K, Heinrich W (2012) The effect of water on intergranular mass transport: new insights from diffusion-controlled reaction rims in the $MgO–SiO_2$ system. Contrib Mineral Petrol 164:1–16

Gardés E, Gaillard F, Tarits P (2014) Toward a unified hydrous olivine electrical conductivity law. Geochem Geophys Geosyst 15:4984–5000

Gardés E, Laumonier M, Massuyeau M, Gaillard F (2020) Unravelling partial melt distribution in the oceanic low velocity zone. Earth Planet Sci Lett 540:116242

Hartmann K, Wirth R, Heinrich W (2010) Synthetic near Σ5 (210)/[100] grain boundary in YAG fabricated by direct bonding: structure and stability. Phys Chem Minerals 37:291–300

Hier-Majumder S, Anderson IM, Kohlstedt DL (2005) Influence of protons on Fe-Mg interdiffusion in olivine. J Geophys Res 110:B02202

Ingrin J, Blanchard M (2006) Diffusion of hydrogen in minerals. Rev Miner Geochem 62:291–320

Jollands MC, Padrón-Navarta JA, Hermann J, O'Neill HSC (2016) Hydrogen diffusion in Ti-doped forsterite and the preservation of metastable point defects. Am Mineral 101:1571–1583

Jollands MC, Zhukova I, O'Neill HSC, Hermann J (2020) Mg diffusion in forsterite from 1250–1600°C. Am Mineral 105:525–537

Kohlstedt DL, Mackwell SJ (1998) Diffusion of hydrogen and intrinsic point defects in olivine. Z Phys Chem 207:147–162

LeClaire AD (1963) The analysis of grain boundary diffusion measurements. J Appl Phys 14:351-356

Le Voyer M, Kelley KA, Cottrell E, Hauri EH (2017) Heterogeneity in mantle carbon content from CO_2-undersaturated basalts. Nat Commun 8:14062

Lide DR (Ed) 2005 CRC Handbook of Chemistry and Physics: A Ready-reference Book of Chemical and Physical Data, 86th Edition. CRC Press

Marquardt K, Faul U H (2018) The structure and composition of olivine grain boundaries: 40 years of studies, status and current developments. Phys Chem Minerals 45:139–172

Massuyeau M, Gardés E, Rogerie G, Aulbach S, Tappe S, Le Trong E, Sifré D, Gaillard F (2021) MAGLAB: A computing platform connecting geophysical signatures to melting processes in Earth's mantle. Phys Earth Planet Inter 314:106638

Milke R, Neusser G, Kolzer K, Wunder B (2013) Very little water is necessary to make a dry solid silicate system wet. Geology 41:247–250

Morrison SM, Downs RT, Flake DF, Prabhu A, Eleish A, Vaniman DT, Ming DW, Rampe EB, Hazen RM, Achilles CN, Treiman AH, Yen AS, Morris RV, Bristow TF, Chipera SJ, Sarrazin PC, Fendrich KV, Morookian JM, Farmer JD, Des Marais DJ, Craig PI (2018) Relationships between unit-cell parameters and composition for rock-forming minerals on Earth, Mars, and other extraterrestrial bodies. Am Mineral 103:848–856

Muir JMR, Jollands MC, Zhang F, Walker AM (2020) Explaining the dependence of M-site diffusion in forsterite on silica activity: a density functional theory approach. Phys Chem Minerals 47:55

Müller G (2007) Review: the Czochralski method - Where we are 90 years after Jan Czochralski's invention. Cryst Res Technol 42:1150–1161

Oelkers EH, Helgeson HC (1988) Calculation of the thermodynamic and transport properties of aqueous species at high pressures and temperatures : Aqueous tracer diffusion coefficients of ions to 1000°C and 5 kb. Geochim Cosmochim Acta 52:63–85

Philibert J (1991) Atom Movements - Diffusion and Mass Transport in Solids, Les Editions de Physique, Les Ulis, Paris

Polednia J, Dohmen R, Marquardt K (2020) Grain boundary diffusion and its relation to segregation of multiple elements in yttrium aluminum garnet. Eur J Mineral 32:675–696

Simpson F, Tommasi A (2005) Hydrogen diffusivity and electrical anisotropy of a peridotite mantle. Geophys J Int 160:1092–1102

Suzuoka T (1961) Lattice and grain boundary diffusion in polycrystals. Trans Jpn Inst Met 2:25–32

Wagner J, Adjaoud O, Marquardt K, Jahn S (2016) Anisotropy of self-diffusion in forsterite grain boundaries derived from molecular dynamics simulations. Contrib Mineral Petrol 171:98

Walker AM, Woodley SM, Slater B, Wright K (2009) A computational study of magnesium point defects and diffusion in forsterite. Phys Earth Planet Inter 172:20–27

Whipple RTP (1954) Concentration contours in grain boundary diffusion. Phil Mag 45:1225–1236

Yoshino T, Matsuzaki T, Shatskiy A, Katsura T (2009) The effect of water on the electrical conductivity of olivine aggregates and its implications for the electrical structure of the upper mantle. Earth Planet Sci Lett 288:291–300

Acknowledgments

We are grateful to M. C. Jollands and an anonymous reviewer for their helpful comments. We thank Y. Buret for trace element analysis at the Imaging and Analysis Centre of the Natural History Museum, London. This work was supported by the French Agence Nationale de la Recherche (ANR) through the projects LabEx EMC3 (ANR-10-LABX-09-01) and EquipEx GENESIS (ANR-11-EQPX-0020)

Ethics declarations

The authors declare that they have no conflict of interest